Supplementary information for

F-regulated Ni2P-F3 nanosheets as efficient electrocatalysts for full-water-splitting and urea oxidation

Xi Sun, ‡[a] Shixue Song, ‡[a] Gaojie Yan, [a] Yingchun Liu ,[b] Huili Ding,[a] Xiaojie Zhang*[a]and Yi Feng*[a]

[a]Hebei Key Laboratory of Functional Polymers, Department of Polymer Materials and Engineering, Hebei University of Technology, Tianjin 300400, P. R. China. Email: zhangxj@hebut.edu.cn (X. Zhang); luckyii0512@hebut.edu.cn (Y. Feng)

[b]Jinghua Plastics Industry Co. Ltd., Langfang 065800, China. Email: jinghuasuye@163.com

Experimental Section

Materials and chemicals

Ammonium fluoride (NH_4F, 96%), Sodium hypophosphite ($NaH_2PO_2 \cdot H_2O$, 98%), Potassium hydroxide (KOH, 99%), acetone(C_3H_6O), urea (CH_4N_2O, 98%), concentrated hydrochloric acid (HCl, 35%) and ethanol (C_2H_6O, 75%) was purchased from Sigma-Aldrich Chemical Reagent Co Ltd. All used reagents were analytical level (A.R.) and used without further purification. Ar (≥ 99.99%) was supplied by Tian Jin Yongcheng Co Ltd. The nickel foam (NF) was purchased from Tian Jin Saibo Co Ltd. Pure water with the resistance of 18.25 $M\Omega \cdot cm^{-1}$ was used throughout all experiments.

Characterizations

A field emission scanning electron microscope (FESEM) (JSM-7610F) and a transmission electron microscope (JEM-2100F) were utilized to observe the morphology of the samples. The samples for the TEM tests were prepared by the ultrasonication of the powdered samples in ethanol and the evaporation of one drop of the suspension onto a carbon film supported on a mesh copper grid. X-ray diffraction (XRD) patterns were obtained by a diffractometer (D8 Discover, AXS) equipped with Cu-Ka radiation of 1.54 Å. All samples were carefully scraped off the substrate for XRD examination. The X-ray photoelectron spectroscopy (XPS) was undertaken on PHI5300 with Mg Ka radiation. All the binding energy for the spectrum was calibrated by C 1s spectrum at 284.8 eV. The in-situ Raman was performed on a Lab RAM HR Evolution Raman microscope using a 532 nm laser with a 50xL objective lens, an acquisition time of 15-30 s and a reduced power of 20 mW.

Electrochemical Characterization

The electrocatalytic water splitting performance of the samples was evaluated using a standard three-electrode system on a CH Instruments electrochemical workstation (760E, CH Instruments, Shanghai, China), with the as-obtained sample (1×1 cm^2) directly used as the working electrode. In the OER process, a platinum sheet and Hg/HgO electrode served as the counter electrode (CE) and reference electrode (RE), respectively, while a graphite counter electrode was used in HER. A 1.0 M KOH (pH = 13.7) solution served as the electrolyte. All potentials were converted to a reversible hydrogen electrode according to the Nernst equation.

$$E_{RHE} = E_{Hg/HgO} + 0.059 \times pH + 0.098 - iR \quad (1)$$

The overpotentials (η) were obtained from:

$$\text{HER: } \eta = E_{RHE} - 0 \quad (2)$$

$$\text{OER: } \eta = E_{RHE} - 1.23 \quad (3)$$

The scan rate for linear sweep voltammetry (LSV) was 2 $mV \cdot s^{-1}$. The Tafel slope were calculated using the equation:

$$\eta = blg|j| + a \quad (4)$$

where b and j represent the Tafel slope ($mV \cdot dec^{-1}$) and current density ($mA \cdot cm^{-2}$), respectively. Electrochemical impedance spectroscopy (EIS) measurements were carried out at the overpotential of 194 mV (vs. RHE) for HER, and the overpotential of 476 mV (vs. RHE) for OER with a frequency range from 10^5 to 0.1 Hz and an amplitude of 10 mV. UOR EIS was obtained at potential of 500 mV. (vs. Hg/HgO) The long-term stability tests were performed by chronoamperometric electrolysis at

50 mA·cm^{-2}. All the measured polarization curves in this work were iR-corrected by the equation (5):

$$E_{cor} = E - iR_s \quad (5)$$

where E_{cor} was the iR-corrected potential, E was the measured potential (*vs.* RHE), i was the current and R_s was the internal resistance (the resistance of the electrolyte/contact between the reference and working electrode) derived from EIS plot.

The electrochemical double-layer capacitance (C_{dl}) of OER, UOR was determined in the potential range of 0.91 ~ 1.01 V vs. RHE according to the CV curve, and HER was calculated in the non-Faradaic potential range of -0.16 ~ -0.06 V vs. RHE according to the following equation.

$$C_{dl} = \frac{j}{v} \quad (6)$$

where C_{dl}, j, and v are the double-layer capacitance (mF·cm^{-2}) of the active materials, charging current (mA·cm^{-2}), and scan rate (mV·s^{-1}), respectively.

The electrochemical active surface area (ECSA) was calculated using the equation:

$$ECSA = \frac{C_{dl}}{Cs} \quad (7)$$

where C_s is the specific capacitance of the electrocatalysts per unit area measured in similar electrolytes. In this study, C_s was taken as 0.040 mF·cm^{-2} on the basis of previously reports. The two-electrode cell for overall water splitting was assembled by employing the Ni_2P-F3 as the anode and cathode. The two-electrode cell was

tested in the 1 M KOH or 1 M KOH with 0.33 M urea.

The onset potential of Ni_2P-F3 in the HER is -50 mV. Ni_2P-F3 had the lowest onset potential of about 125 mV in the OER.

The turnover frequency (TOF) values were calculated as the number of oxygen molecules evolved per active site per second based on the following equation:

$$TOF = \frac{J \times A}{4 \times F \times m} \quad (8)$$

The current density "J" ($A \cdot cm^{-2}$) obtained at overpotential of 300 mV. The effective surface geometric area "A" (1 cm^2) of the working electrode, Faradaic efficiency "F" (96485 s $A \cdot mol^{-1}$), and the number of moles "m" of the active metal on the electrode, which is determined by the XPS results.

The number of moles (m) is calculated from XPS results: Ni_2P (active metal is Ni): atomic percentage: Ni 66.89 %, P 33.11 %.

Loading of Ni_2P was about 2.69 $mg \cdot cm^{-2}$. We set total mols of Ni, P as X, we could get:

$55.85 \times 0.6689\ X + 31 \times 0.3311\ X = 2.69 \times 10^{-3}$

$m = 0.6689\ X = 3.63 \times 10^{-5}$ g

According to LSV curve, the current density is 0.01159 $A \cdot cm^{-2}$ when the overpotential of 300 mV.

$TOF = 8.27 \times 10^{-4}\ s^{-1}$

To compare the intrinsic activity of catalysts, the turnover frequency (TOF) values were calculated based on XPS data and LSV curves. The TOF of Ni_2P-F3 is $5.16 \times 10^{-3}\ s^{-1}$ at an overpotential of 300 mV, which is higher than that of Ni_2P (8.27

$\times 10^{-4}$ s^{-1}), indicating that Ni_2P-F3 has excellent electrocatalytic properties.

Steady-state Tafel Polarization curves are evaluated by sampling current density at 360th second of chronoamperometry responses. The chronoamperometry measurements are conducted with the interval of 10 mV (HER) and 20 mV (OER and UOR).

Computational details

Density functional theory (DFT) calculations were performed using the Vienna Ab Initio Simulation Package (VASP). Exchange-correlation energies were determined by using the Perdew–Burke–Ernzerhof (PBE) model of generalized gradient approximation (GGA). The k-points (Monkhorst-Pack method), energy cutoff, and self-consistent field energy convergence was set to 4×4×1, 520 eV, and 1×10^{-6} eV, respectively. Then, frequency calculations of these structures were performed at the same level. After this, vaspkit 1.3.0 was utilized to calculate Gibbs free energies of these structures [1]. Besides that, density of states and band gap were also calculated at the same level with the optimization process.

The oxygen evolution reactions in alkaline medium involves the four proton-transfer steps: [2,3]

$$^{*} + OH^{-} \rightarrow OH^{*} + e^{-} \quad (8)$$

$$OH^{*} + OH^{-} \rightarrow O^{*} + H_2O + e^{-} \quad (9)$$

$$O^{*} + OH^{-} \rightarrow OOH^{*} + e^{-} \quad (10)$$

$$OOH^{*} + OH^{-} \rightarrow O^2 + H^2O + e^{-} \quad (11)$$

where the * represents the active site when OER occurred, and the OH*, O*, and

OOH* represent the intermediate species adsorbed on the active sites. For each step, the reaction free energy (ΔG_{OER}) is calculated by

$$\Delta G_{OER} = \Delta E + \Delta ZPE - T\Delta S \quad (12)$$

where, ΔE, ΔZPE, and ΔS are the difference in total energy, zero-point energy, and entropy between final and initial states, respectively, and T is the temperature at 298.15 K. Zero-point energies for the OER intermediates were obtained from the vibrational frequencies after structural optimization and those of free gas-phase molecules were obtained from thermodynamics database[4]. While for the intermediates adsorbed on the surface, the entropy was set to zero since intermediates lose the translational and rotational degrees of freedom upon adsorption, which had been proved to be a good approximation in the previous theoretical reports[5]. The energies of H_2O and H_2 in the gas phase by DFT were used as references states because they are well described within DFT [6]. Since oxygen molecule has a complicated electronic structure which cannot be described accurately by DFT, the free energy change of the total reaction ($H_2O \rightarrow 1/2O_2 + H_2$) is fixed in this work to avoid the direct calculation of O_2 molecule. The value for the total reaction is found to be 2.46 eV. Hence,

$$G_{O_2} = 4.92 - 2\,E_{H_2} + 2E_{H_2O} - (\Delta ZPE - T\Delta S)_{2H_2O \rightarrow O_2 + 2H_2} \quad (13)$$ [4,7]

It is worth noting that the ΔG4 is calculated by 4.92 – ΔG_3 – ΔG_2 – ΔG_1 to avoid calculating the O_2 adsorption and desorption[7].

The DFT calculations of HER were modeled in the same way as OER. The hydrogen-metal interaction plays an essential role in HER occurred on the metal surface. A typical descriptor of the rate of the overall reaction is the adsorption free energy of H

and expressed as follows equation:

The hydrogen adsorption free energy ΔG_{H*} is calculated by

$$\Delta G_{H*} = E_{slab+H} - E_{slab} - \frac{1}{2}E_{H_2} + \Delta ZPE - T\Delta S \quad (14)$$

where E_{slab+H} and E_{slab} represent the energy of total system with and without one adsorbed H atom, respectively, and E_{H_2} is the energy of H_2 gas molecules. ΔZPE and ΔS are the difference in the zero-point energy and entropy between the adsorbed H atom and the gaseous phase H_2. According to the reports of Norskov et al, the value of ΔZPE–TΔS is approximately equal to 0.24 eV at T=300 K[8]. Hence, ΔG_{H*} can be calculated by

$$\Delta G_{H*} = E_{slab+H} - E_{slab} - \frac{1}{2}E_{H_2} + 0.24 \quad (15)$$

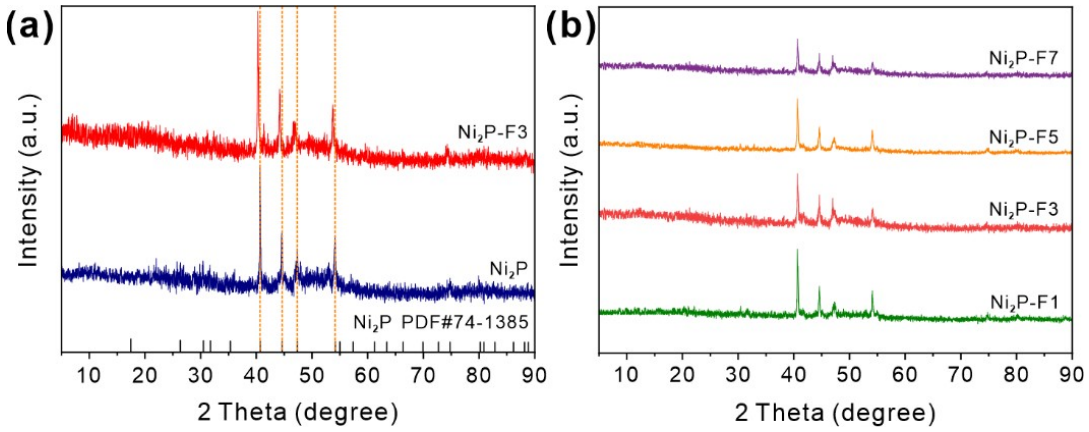

Fig. S1 XRD pattern of (a) Ni_2P and Ni_2P-F3 (b) Ni_2P–F1, Ni_2P-F3, Ni_2P-F5 and Ni_2P-F7.

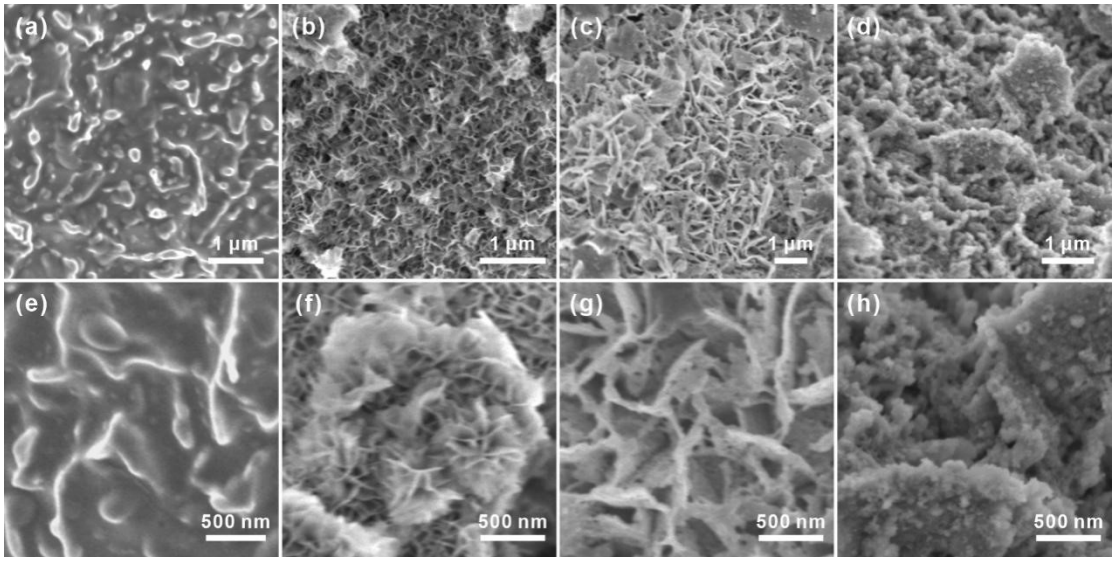

Fig. S2 SEM images of (a, e) Ni_2P; (b, f) Ni_2P-F1; (c, g) Ni_2P-F5 and (d, h) Ni_2P-F7 with different magnifications

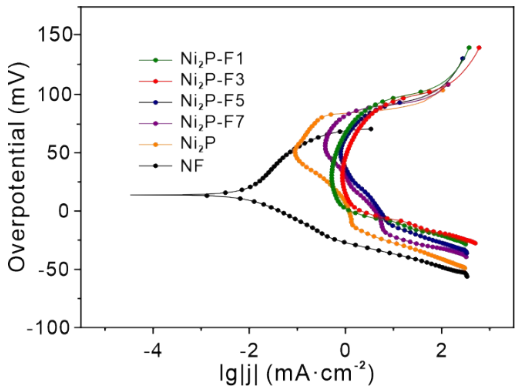

Fig. S3 Steady-state Tafel Plots of HER.

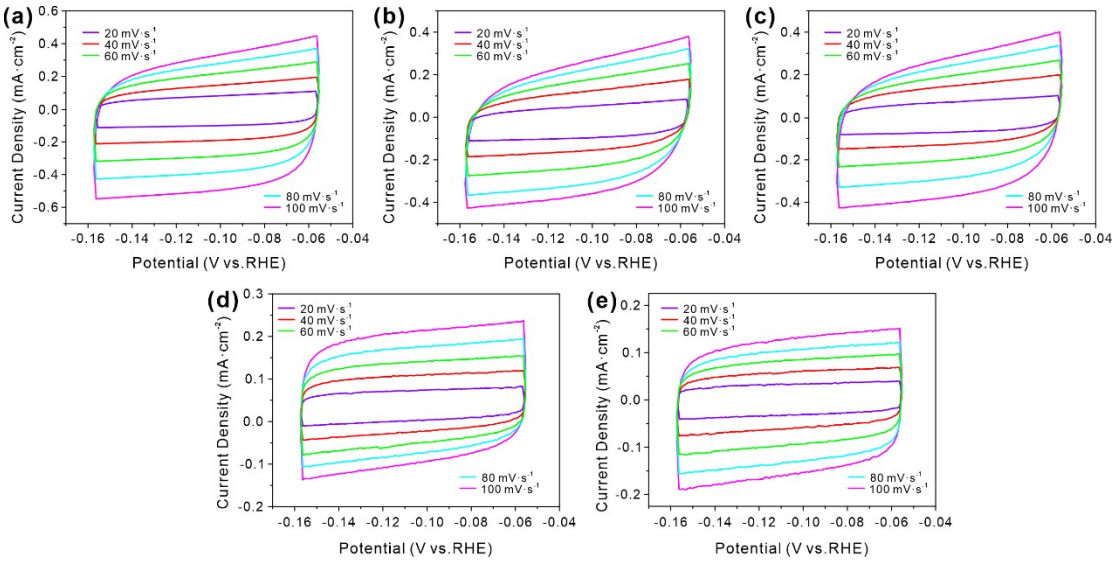

Fig. S4 HER Cyclic Voltammetry curves of (a) Ni_2P–F3, (b) Ni_2P–F1, (c) Ni_2P–F5 (d) Ni_2P–F7 (e) Ni_2P measured in the non-Faradaic potential range (-0.16 ~ -0.06 V vs. RHE) at scan rates of 20, 40, 60, 80, 100 mV s^{-1}, respectively

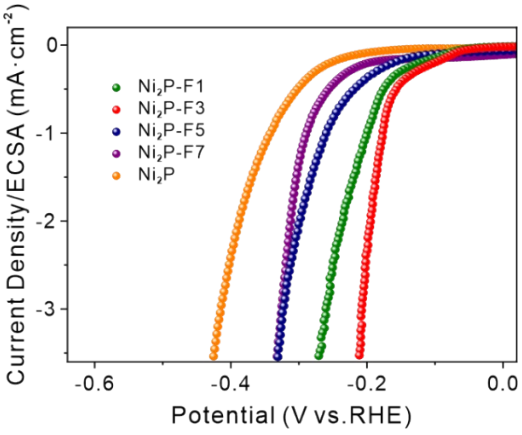

Fig. S5 ECSA normalised LSV curves of HER.

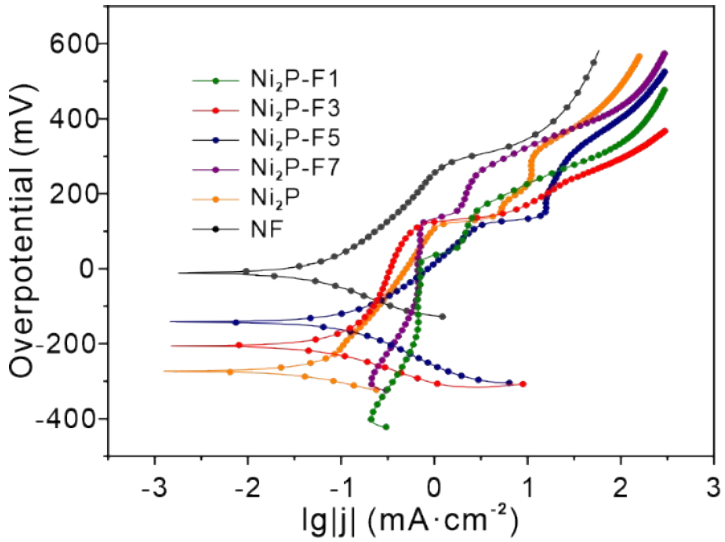

Fig. S6 Steady-state Tafel Plots of OER.

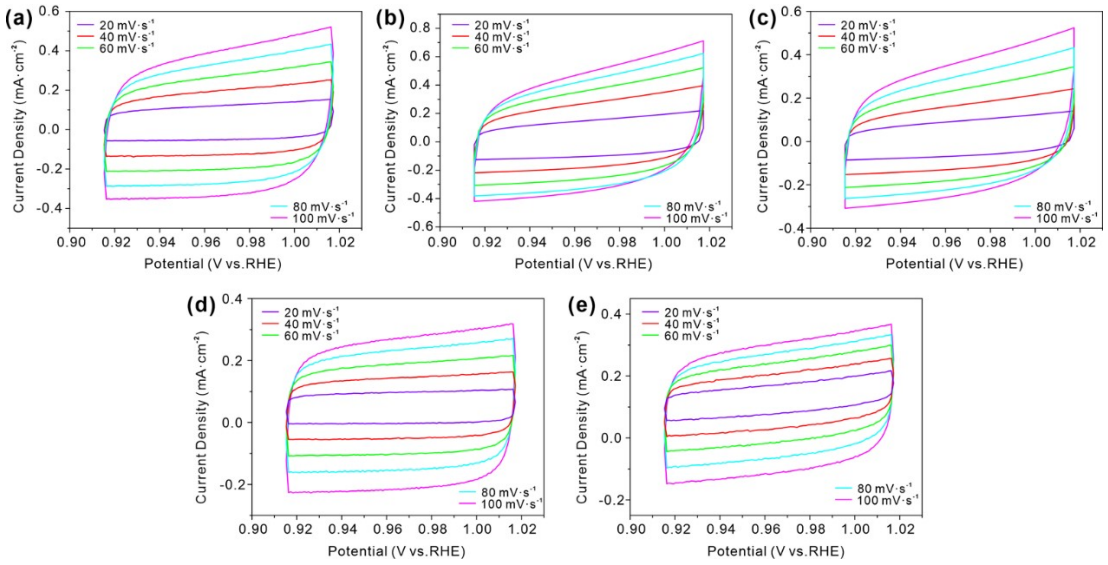

Fig. S7 OER Cyclic Voltammetry curves of (a) Ni_2P–F3, (b) Ni_2P–F1, (c) Ni_2P–F5 (d) Ni_2P–F7 (e) Ni_2P measured in the non-Faradaic potential range (0.91 ~ 1.01 V vs. RHE) at scan rates of 20, 40, 60, 80, 100 mV s^{-1}, respectively.

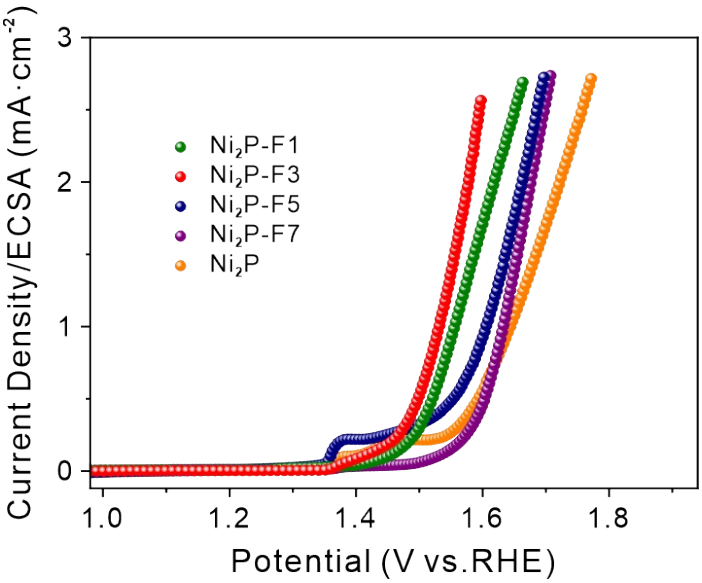

Fig. S8 ECSA normalised LSV curves of OER .

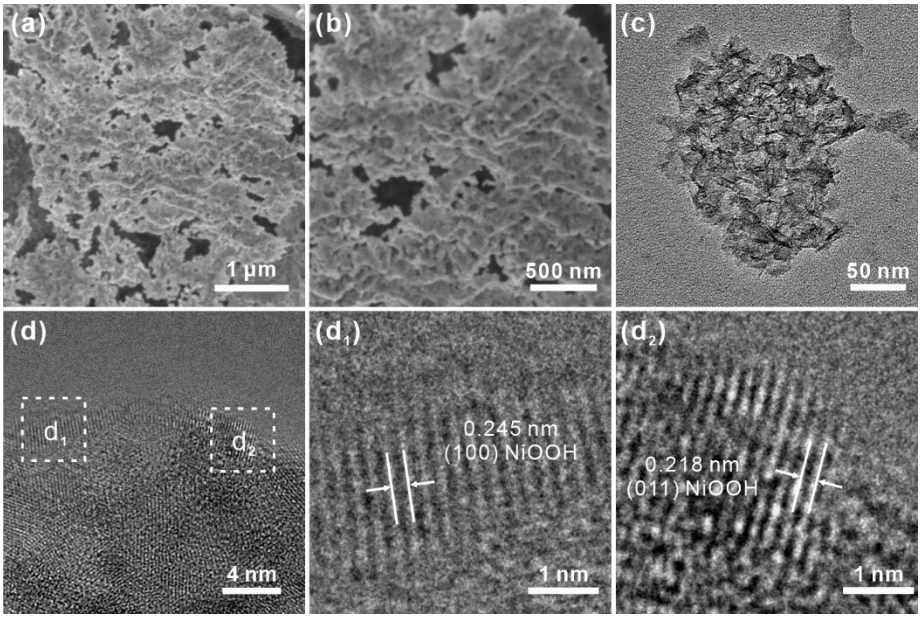

Fig. S9 (a,b) SEM with different magnifications;(c) TEM and (d-d$_2$) HRTEM image with different magnifications of Ni$_2$P-F3 after OER stability test.

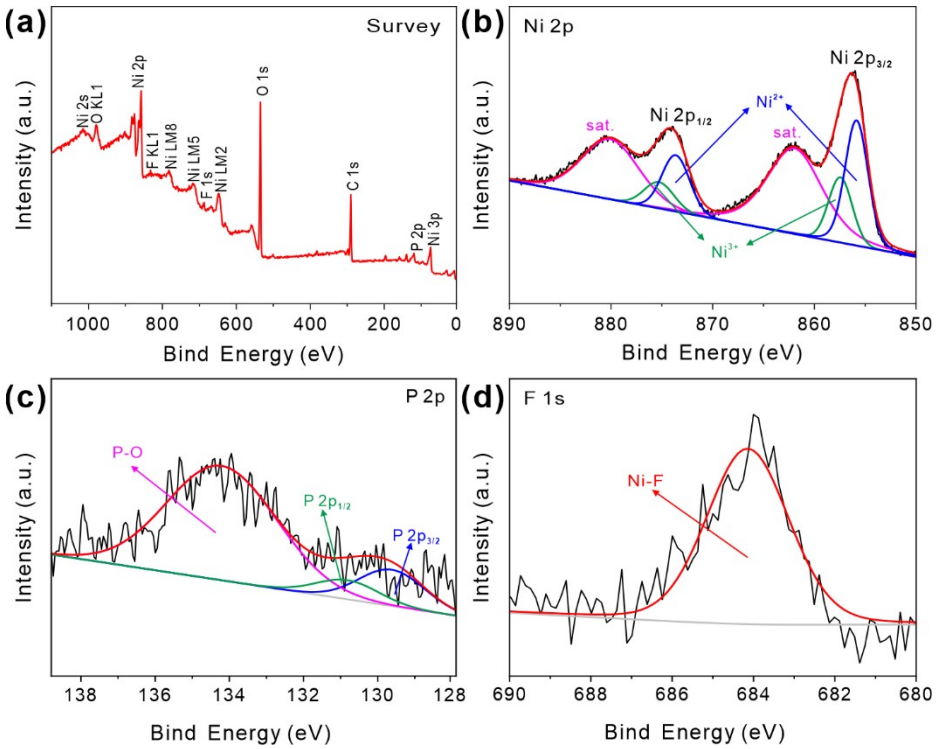

Fig. S10 XPS spectrum of Ni_2P-F3 after OER stability test: (a) survey; (b-d) high resolution spectra of Ni 2p, P 2p and F 1s, respectively.

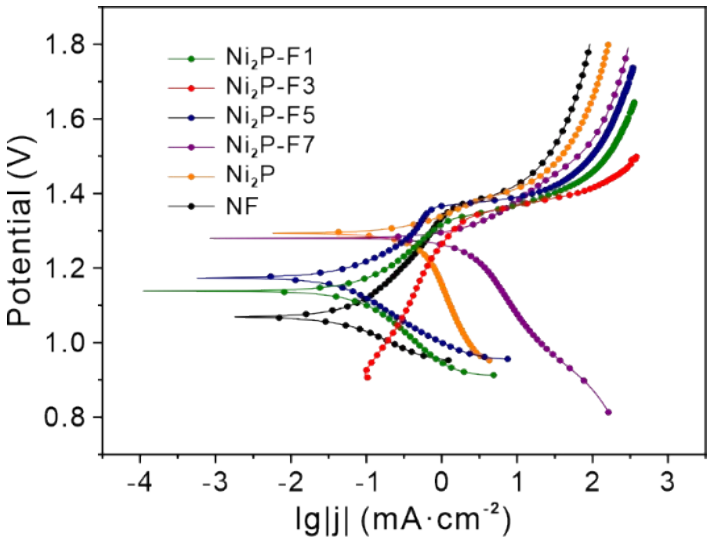

Fig. S11 Steady-state Tafel Plots of UOR.

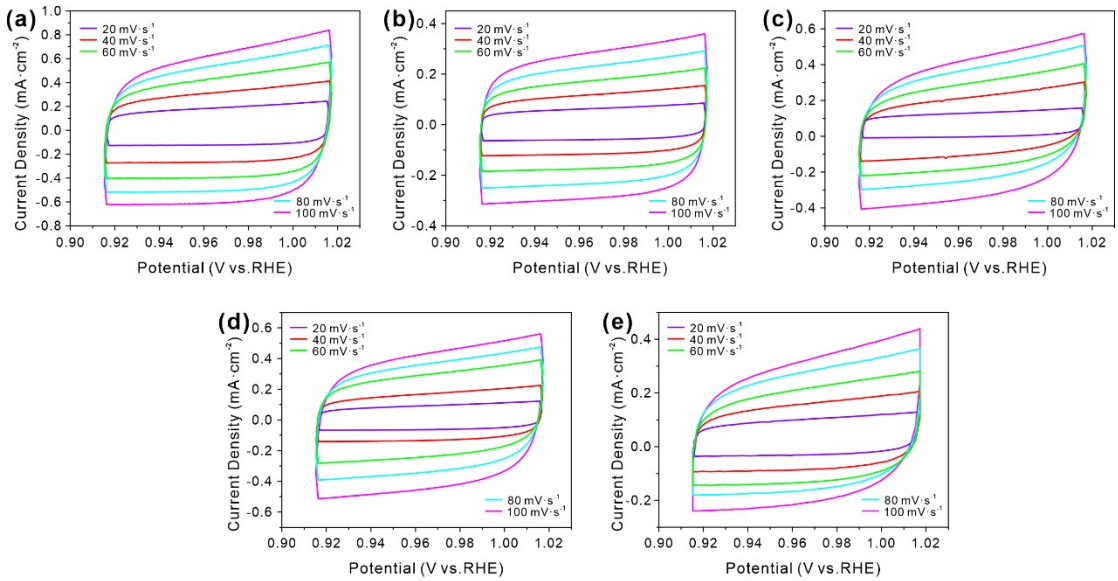

Fig. S12 UOR Cyclic Voltammetry curves of (a) Ni_2P–F3, (b) Ni_2P–F1, (c) Ni_2P–F5 (d) Ni_2P–F7 (e) Ni_2P measured in the non-Faradaic potential range (0.91 ~ 1.01 V vs. RHE) at scan rates of 20, 40, 60, 80, 100 mV s^{-1}, respectively.

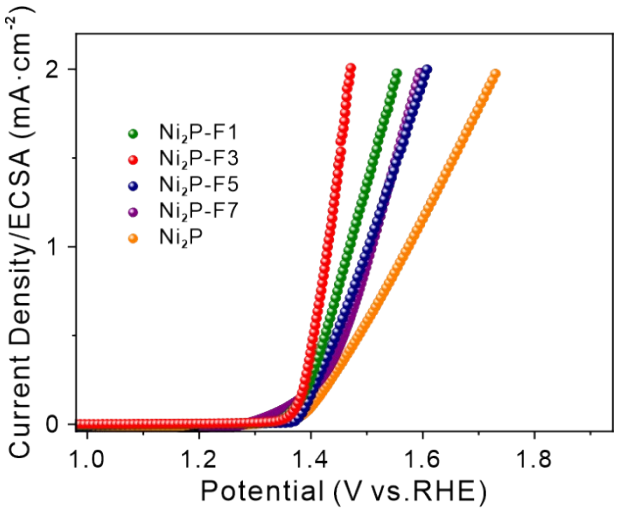

Fig. S13 ECSA normalised LSV curves of UOR

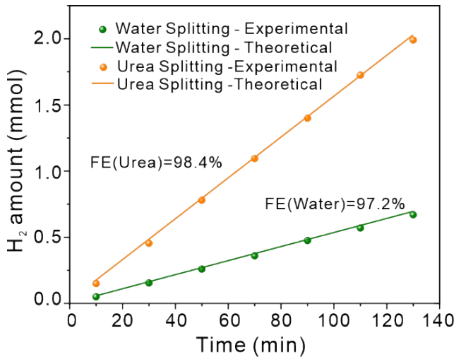

Fig. S14 Faradaic efficiencies of Urea assisted HER and water-splitting (Faradaic efficiencyies are measured under the voltage of 1.8 V).

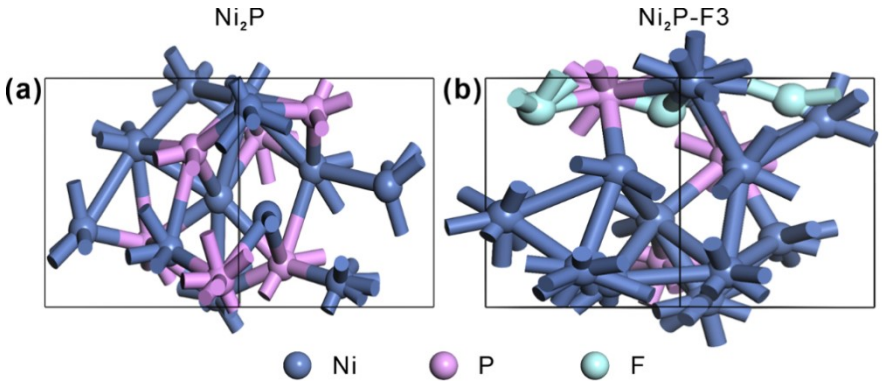

Fig. S15 The crystal structure of (a) Ni_2P and (b) Ni_2P-F3.

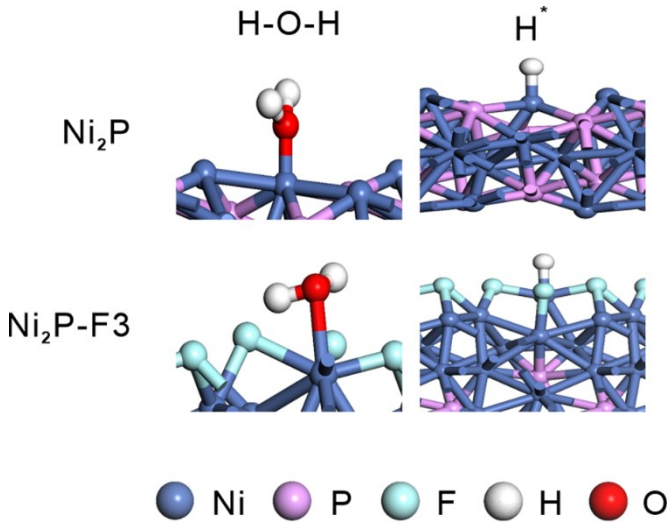

Fig. S16 Optimized theoretical models for the H_2O and H* adsorbed on the surface of on Ni_2P and Ni_2P-F3.

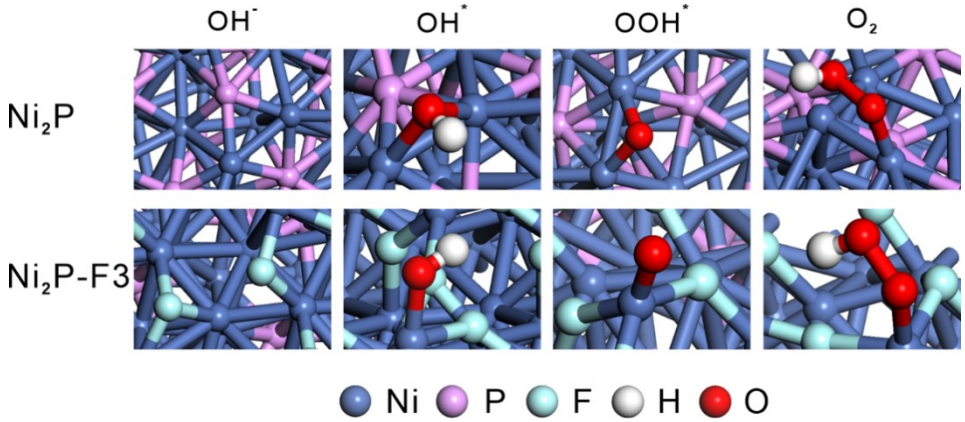

Fig. S17 Surface configurations of dissociating process of H_2O and adsorption/desorption of oxygen intermediate on Ni_2P and Ni_2P-F3

Table S1 F and P contents of the samples in Fig. 3 measured by XPS.

samples	Atomic Percentage (at %)			Atomic ratio
	Ni	P	F	Ni/P or Ni/(P+F)
Ni_2P	66.89	33.11	/	Ni/P=2.00
Ni_2P-F3	64.45	26.47	9.08	Ni/(P+F) =1.81

Table S2 The HER performance of recently reported Ni-based electrocatalysts.

Catalyst	Measurement	*J* (mA cm^{-2})	*η* (mV)	Tafel slope (mV dec^{-1})	Ref.
Ni_2P-F3 electrocatalyst	**Ni foam 1.0 M KOH**	**-10/-100**	**92/210**	**43.1**	**This work**
F-FeCoNi-Ov LDH/NF	Ni foam 1.0 M KOH	-10	109.8	83.8	[9]
N,F-GQDs	Ni foam 1.0 M KOH	-10	130	/	[10]
Fe-Mo-S/Ni_3S_2@ NF	Ni foam 1.0 M KOH	-10	141	123	[11]
CoSx/Ni_3S_2@NF	Ni foam 1.0 M KOH	-10	204	113.13	[12]
NiFeSP/NF	Ni foam 1.0 M KOH	-10	91	82.6	[13]
NiS/Ni-120	Ni foam 1.0 M KOH	-10	162	74	[14]
NiS/NiS_2	Carbon cloth 1.0 M KOH	-100	248	95.1	[15]
NiP/NF	Ni foam 1.0 M KOH	-10	102	90	[16]
ReS_2-$F_{5.93}$	Powder 1.0 M NaOH	-10	142	64	[17]
F-NiPx/ Ni_3S_2-NF	Ni foam 1.0 M KOH	-100	182	83	[18]

Table S3 The OER performance of recently reported Ni-based electrocatalysts.

Catalyst	Measurement	J (mA cm^{-2})	η (mV)	Tafel slope (mV dec^{-1})	Ref.
Ni_2P-F3 electrocatalyst	**Ni foam 1.0 M KOH**	**100**	**293**	**51.72**	**This work**
F-Ni_3S_2	Ni foam 1.0 M KOH	100	310	36	[19]
F-NiPx/ Ni_3S_2-NF	Ni foam 1.0 M KOH	100	370	92	[18]
NiP/NF	Ni foam 1.0 M KOH	100	360	78	[16]
NiS/NiO@N-C NT/NFs	Ni foam 1.0 M KOH	100	about 410	48.4	[20]
NiS/Ni-90	Ni foam 1.0 M KOH	30	338	46	[14]
F-CoOOH/NF	Ni foam 1.0 M NaOH	50	310	54	[21]
$Ni(OH)_2$/F-Ni_3S_2/NF(FN-20)	Ni foam 1.0 M KOH	100	360	126	[9]
F-FeCoNi-Ov LDH/NF	Ni foam 1.0 M KOH	100	265	57.82	[22]
Fe-Ni-F-150	Ni foam 1.0 M KOH	100	370	79	[23]
NiS/NiS_2	Carbon cloth 1.0 M KOH	100	416	38.8	[15]
NiSP-NF	Ni foam 1.0 M KOH	50	341	99	[24]

Table S4 The UOR performance of recently reported Ni-based electrocatalysts.

Catalyst	Measurement	*J* (mA cm^{-2})	*η* (mV)	Ref.
Ni_2P-F3 / Ni_2P-F3	**Ni foam 1.0 M KOH+0.33 M urea**	**100/50**	**1.414/1.395**	**This work**
O-NiMoP	Ni foam 1.0 M KOH+0.5 M urea	100	1.41	[25]
CA-Ni_5P_4@NiOx/NF	Ni foam 1.0 M KOH+0.33 M urea	100	1.45	[26]
N-NiS/NiS_2	powder 1.0 M KOH+0.33 M urea	100	1.47	[27]
NiFeCo LDH	Ni foam 1.0 M KOH+0.33 M urea	100	about 1.416	[28]
$NiCo_2S_4$ NS	carbon cloth 1.0 M KOH+0.33 M urea	100	about 1.546	[29]
Fe11.1%Ni_3S_2	Ni foam 1.0 M KOH+0.33 M urea	100	1.438	[30]
Ni $(OH)_2$	powder 1.0 M KOH+0.33 M urea	10	1.518	[31]
V-$FeNi_3N$/Ni_3N	Ni foam 1.0 M KOH+0.33 M urea	100	1.42	[32]

Table S5 The overall water splitting performance of recently reported Ni-based electrocatalysts.

Catalyst	Measurement	*J* (mA cm^{-2})	*η* (mV)	Ref.
Ni_2P-F3 / Ni_2P-F3	**Ni foam 1.0 M KOH**	**10**	**1.618**	**This work**
NiP/NF / NiP/NF	Ni foam 1.0 M KOH	10	1.63	[16]
CoFe/NF / CoFe/NF	Ni foam 1.0 M KOH	10	1.64	[33]
MoP/ NF / MoP/ NF	Ni foam 1.0 M KOH	10	1.62	[34]
$Co_5Mo_{1.0}O$ NSs@NF / $Co_5Mo_{1.0}P$ NSs@NF	Ni foam 1.0 M KOH	10	1.68	[35]
CuSe/NF / CuSe/NF	Ni foam 1.0 M KOH	10	1.68	[36]
$Ni_{0.5}Co_{0.5}$/NC / $Ni_{0.5}Co_{0.5}$/NC	Powder 1.0 M KOH	10	1.75	[37]
NiFe/NF / NiFe/NF	Ni foam 1.0 M KOH	10	1.64	[38]
Pt@Co_3O_4/NF / Pt@Co_3O_4/NF	Ni foam 1.0 M KOH	10	1.53	[39]

Table S6 The urea assisted overall water splitting performance of recently reported Ni-based electrocatalysts.

Catalyst	Measurement	*J* (mA cm^{-2})	*η* (mV)	Ref.
Ni_2P-F3 / Ni_2P-F3	**Ni foam 1.0 M KOH+0.33 M urea**	**10**	**1.458**	**This work**
NiFeCo LDH / NF / NiFeCo LDH / NF	Ni foam 1.0 M KOH+0.33 M urea	10	1.49	[28]
V-$FeNi_3N$/Ni_3N / V-$FeNi_3N$/Ni_3N	Ni foam 1.0 M KOH+0.33 M urea	10	1.46	[32]
CoFe-250 / CoFe-250	Ni foam 1.0 M KOH+0.33 M urea	10	1.47	[40]
Ni@NCNT / Ni@NCNT	Ni foam 1.0 M KOH+0.33 M urea	10	1.56	[41]
Ni_3S_2−H_2|Ni_3S_2−Ar / Ni_3S_2−H_2|Ni_3S_2−Ar	Ni foam 1.0 M KOH+0.33 M urea	10	about 1.48	[42]
CA-Ni_5P_4@NiOx/NF / CA-Ni_5P_4@NiOx/NF	Ni foam 1.0 M KOH+0.33 M urea	10	1.52	[26]
Ce-Ni_2P/NF / Ce-Ni_2P/NF	Ni foam 1.0 M KOH+0.33 M urea	10	1.51	[43]
NiFeRh-LDH / NiFeRh-LDH	Ni foam 1.0 M KOH+0.33 M urea	10	1.455	[44]

Supplementary references

1 V. Wang, N. Xu, J.-C. Liu, G. Tang and W.-T. Geng, *Computer Physics Communications*, 2021, **267**, 108033.

2 E. Skúlason, V. Tripkovic, M. E. Björketun, S. Gudmundsdóttir, G. Karlberg, J. Rossmeisl, T.

Bligaard, H. Jónsson and J. K. Nørskov, *J. Phys. Chem. C*, 2010, **114**, 22374–22374.
3 X. Luo, P. Ji, P. Wang, R. Cheng, D. Chen, C. Lin, J. Zhang, J. He, Z. Shi, N. Li, S. Xiao and S. Mu, *Advanced Energy Materials*, 2020, **10**, 1903891.
4 S. Lin, X. Ye, X. Gao and J. Huang, *Journal of Molecular Catalysis A: Chemical*, 2015, **406**, 137–144.
5 J. Rossmeisl, A. Logadottir and J. K. Nørskov, *Chemical Physics*, 2005, **319**, 178–184.
6 J. K. Nørskov, J. Rossmeisl, A. Logadottir, L. Lindqvist, J. R. Kitchin, T. Bligaard and H. Jónsson, *J. Phys. Chem. B*, 2004, **108**, 17886–17892.
7 Y. Bi, Z. Cai, D. Zhou, Y. Tian, Q. Zhang(m), Q. Zhang(f), Y. Kuang, Y. Li, X. Sun and X. Duan, *Journal of Catalysis*, 2018, **358**, 100–107.
8 J. K. Nørskov, T. Bligaard, A. Logadottir, J. R. Kitchin, J. G. Chen, S. Pandelov and U. Stimming, *J. Electrochem. Soc.*, 2005, **152**, J23.
9 P. Hao, W. Zhu, F. Lei, X. Ma, J. Xie, H. Tan, L. Li, H. Liu and B. Tang, *Nanoscale*, 2018, **10**, 20384–20392.
10 Y. Sim, S. J. Kim, G. Janani, Y. Chae, S. Surendran, H. Kim, S. Yoo, D. C. Seok, Y. H. Jung, C. Jeon, J. Moon and U. Sim, *Applied Surface Science*, 2020, **507**, 145157.
11 Y. Zhang, H. Guo, X. Li, J. Du, W. Ren and R. Song, *Chemical Engineering Journal*, 2021, **404**, 126483.
12 S. Shit, S. Chhetri, W. Jang, N. C. Murmu, H. Koo, P. Samanta and T. Kuila, *ACS Appl. Mater. Interfaces*, 2018, **10**, 27712–27722.
13 Y. Xin, X. Kan, L.-Y. Gan and Z. Zhang, *ACS Nano*, 2017, **11**, 10303–10312.
14 C. Yan, J. Huang, C. Wu, Y. Li, Y. Tan, L. Zhang, Y. Sun, X. Huang and J. Xiong, *Journal of Materials Science & Technology*, 2020, **42**, 10–16.
15 Q. Li, D. Wang, C. Han, X. Ma, Q. Lu, Z. Xing and X. Yang, *J. Mater. Chem. A*, 2018, **6**, 8233–8237.
16 J. Ren, Z. Hu, C. Chen, Y. Liu and Z. Yuan, *Journal of Energy Chemistry*, 2017, **26**, 1196–1202.
17 Y. Liu, H. Li, J. Li, X. Ma, Z. Cui, D. Gao and Z. Tang, *J. Mater. Chem. A*, 2021, **9**, 14451–14458.
18 K. Li, Y. Tong, D. Feng and P. Chen, *Journal of Colloid and Interface Science*, 2022, **625**, 576–584.
19 Q. Xu, M. Chu, M. Liu, J. Zhang, H. Jiang and C. Li, *Chemical Engineering Journal*, 2021, **411**, 128488.
20 T. Li, T. Lu, Y. Li, J. Yin, Y. Tang, M. Zhang, H. Pang, L. Xu, J. Yang and Y. Zhang, *Chemical Engineering Journal*, 2022, **428**, 131094.
21 P. Chen, T. Zhou, S. Wang, N. Zhang, Y. Tong, H. Ju, W. Chu, C. Wu and Y. Xie, *Angew Chem Int Ed*, 2018, **57**, 15471–15475.
22 Z. Zhai, W. Yan and J. Zhang, *Nanoscale*, 2022, **14**, 4156–4169.
23 C. Pei, Y. Gu, Z. Liu, X. Yu and L. Feng, *ChemSusChem*, 2019, **12**, 3849–3855.
24 R. A. Marquez-Montes, K. Kawashima, Y. J. Son, J. A. Weeks, H. H. Sun, H. Celio, V. H. Ramos-Sánchez and C. B. Mullins, *J. Mater. Chem. A*, 2021, **9**, 7736–7749.
25 H. Jiang, M. Sun, S. Wu, B. Huang, C. Lee and W. Zhang, *Adv Funct Materials*, 2021, **31**, 2104951.
26 Z. Ma, H. Wang, H. Ma, S. Zhan and Q. Zhou, *Fuel*, 2022, **315**, 123279.

27 H. Liu, Z. Liu, F. Wang and L. Feng, *Chemical Engineering Journal*, 2020, **397**, 125507.
28 P. Babar, A. Lokhande, V. Karade, B. Pawar, M. G. Gang, S. Pawar and J. H. Kim, *ACS Sustainable Chem. Eng.*, 2019, **7**, 10035–10043.
29 W. Zhu, M. Ren, N. Hu, W. Zhang, Z. Luo, R. Wang, J. Wang, L. Huang, Y. Suo and J. Wang, *ACS Sustainable Chem. Eng.*, 2018, **6**, 5011–5020.
30 W. Zhu, Z. Yue, W. Zhang, N. Hu, Z. Luo, M. Ren, Z. Xu, Z. Wei, Y. Suo and J. Wang, *J. Mater. Chem. A*, 2018, **6**, 4346–4353.
31 X. Zhu, X. Dou, J. Dai, X. An, Y. Guo, L. Zhang, S. Tao, J. Zhao, W. Chu, X. C. Zeng, C. Wu and Y. Xie, *Angew Chem Int Ed*, 2016, **55**, 12465–12469.
32 J. Wang, Y. Sun, Y. Qi and C. Wang, *ACS Appl. Mater. Interfaces*, 2021, **13**, 57392–57402.
33 P. Babar, A. Lokhande, H. H. Shin, B. Pawar, M. G. Gang, S. Pawar and J. H. Kim, *Small*, 2018, **14**, 1702568.
34 Y. Jiang, Y. Lu, J. Lin, X. Wang and Z. Shen, *Small Methods*, 2018, **2**, 1700369.
35 Y. Zhang, Q. Shao, S. Long and X. Huang, *Nano Energy*, 2018, **45**, 448–455.
36 B. Chakraborty, R. Beltrán‐Suito, V. Hlukhyy, J. Schmidt, P. W. Menezes and M. Driess, *ChemSusChem*, 2020, **13**, 3222–3229.
37 B. Bayatsarmadi, Y. Zheng, V. Russo, L. Ge, C. S. Casari and S.-Z. Qiao, *Nanoscale*, 2016, **8**, 18507–18515.
38 Q. Luo, M. Peng, X. Sun, Y. Luo and A. M. Asiri, *International Journal of Hydrogen Energy*, 2016, **41**, 8785–8792.
39 L. Huang, M. Wei, S. Zaman, A. Ali and B. Y. Xia, *Chemical Engineering Journal*, 2020, **398**, 125669.
40 Q. Zhang, M. Sun, J. Zhu, S. Yang, L. Chen, X. Yang, P. Wang, K. Li, F. Xue, Y. Lu, J. Zhang and P. Zhao, *Chemical Engineering Journal*, 2022, **432**, 134275.
41 Q. Zhang, F. Md. Kazim, S. Ma, K. Qu, M. Li, Y. Wang, H. Hu, W. Cai and Z. Yang, *Applied Catalysis B: Environmental*, 2021, **280**, 119436.
42 Y. Zhang, Y. Qiu, Y. Wang, B. Li, Y. Zhang, Z. Ma and S. Liu, *ACS Appl. Mater. Interfaces*, 2021, **13**, 3937–3948.
43 K. Xiong, L. Yu, Y. Xiang, H. Zhang, J. Chen and Y. Gao, *Journal of Alloys and Compounds*, 2022, **912**, 165234.
44 H. Sun, W. Zhang, J.-G. Li, Z. Li, X. Ao, K.-H. Xue, K. K. Ostrikov, J. Tang and C. Wang, *Applied Catalysis B: Environmental*, 2021, **284**, 119740.